JGR Atmospheres

RESEARCH ARTICLE
10.1029/2020JD032429

Special Section:
Integrative Monsoon Frontal Rainfall Experiment

Key Points:
- An event that produced a historical amount of rainfall in Wuhan during the Meiyu period is reviewed
- Riming and aggregation processes were enhanced as the cloud system moved out of the Tibetan Plateau
- The event was dominated by an eastward moving system acting as "seeder" cloud, together with the increasing water vapor acting as "feeder" cloud

Correspondence to:
Y. Fu,
fyf@ustc.edu.cn

Citation:
Chen, Y., Zhang, A., Zhang, Y., Cui, C., Wan, R., Wang, B., & Fu, Y. (2020). A heavy precipitation event in the Yangtze River Basin led by an eastward moving Tibetan Plateau cloud system in the summer of 2016. *Journal of Geophysical Research: Atmospheres*, *125*, e2020JD032429. https://doi.org/10.1029/2020JD032429

Received 26 JAN 2020
Accepted 3 JUN 2020
Accepted article online 22 JUL 2020

A Heavy Precipitation Event in the Yangtze River Basin Led by an Eastward Moving Tibetan Plateau Cloud System in the Summer of 2016

Yilun Chen[1,2,3], Aoqi Zhang[1,2,3], Yuheng Zhang[1], Chunguang Cui[4], Rong Wan[4], Bin Wang[4], and Yunfei Fu[1,4]

[1]School of Earth and Space Sciences, University of Science and Technology of China, Hefei, China, [2]School of Atmospheric Sciences, Sun Yat-sen University, Zhuhai, China, [3]Southern Marine Science and Engineering Guangdong Laboratory (Zhuhai), Zhuhai, China, [4]Hubei Key Laboratory for Heavy Rain Monitoring and Warning Research, Institute of Heavy Rain, China Meteorological Administration, Wuhan, China

Abstract From 29 June to 6 July 2016, China's Yangtze River Basin experienced heavy precipitation, causing more than 200 deaths and affecting tens of millions of people. Using ERA5 reanalysis, soundings, and satellite observations from FY-2 and Global Precipitation Measurement (GPM), we reviewed this heavy rainfall event from the perspective of its meteorological triggers and the cloud microphysics. As the cloud system moved eastward from the Tibetan Plateau, precipitation particles got larger and denser, and the enhancement of stratiform precipitation contributed the most precipitation. The riming and aggregation processes, the dominant growth modes of particles, were significantly enhanced between 5.5 and 7 km. The increase in the echo-top height had a considerable positive effect on the near-surface particle size (from ~1.0 mm at 4 km to ~1.5 mm at 10 km), but this feature was not significant over the Tibetan Plateau. We suggest that the microphysics of this event was dominated by the combination of the eastward moving cloud system, which acted as continuous "seeder" cloud, and the increase in water vapor associated with the low-level vortex and jet, which generated enhancing "feeder" cloud. The particles from the "seeder" cloud grew by the lower "feeder" cloud, thus increasing the particle size to enhance the precipitation. Overall, the generation and movement of such a cloud system is an important atmospheric disturbance for the generation of heavy precipitation downstream, and could be an early warning signal in the forecasting of heavy rainfall in China during the Meiyu period.

1. Introduction

As the highest and largest plateau in the world, the Tibetan Plateau maintains water vapor transport in the surrounding areas and influences the atmospheric circulation via both orographic and thermal forcings (Y. Liu et al., 2007; Wu et al., 2012; Xu et al., 2008). Recent studies have revealed the unique cloud (precipitation) vertical structures and their generation mechanisms over the Tibetan Plateau and its surrounding areas from a statistical perspective (Y. Chen et al., 2017; Fu et al., 2018, 2020; Y. Li et al., 2006; L. Liu et al., 2015; Luo et al., 2011; Yan et al., 2016, 2018; A. Zhang et al., 2018).

Mesoscale convective systems (MCSs) are usually generated in a strongly unstable environment, and are accompanied by both convective and stratiform precipitation (Houze, 2004). They are closely linked to precipitation in the Tibetan Plateau and adjacent areas (Houze et al., 2017; Luo et al., 2014; Luo & Chen, 2015). Due to the strong solar heating over the Tibetan Plateau in summer, MCS generation has been observed by many researches (Barros et al., 2004; Fu et al., 2006; Houze et al., 2007). However, the study on the linkage of MCSs between Tibetan Plateau and adjacent areas is still lacking, especially from the aspect of cloud physics.

China is situated in a monsoon-affected area, affected by both cold air from the higher latitudes and the monsoon from the south in summer. The combination helps form a "Meiyu" front over the Yangtze River Basin, which initiates and maintains persistent precipitation, sometimes causes catastrophic flooding (Ding, 1992). The heavy precipitation during the Meiyu period is related to many factors. For example, low-level vortices originating over the Tibetan Plateau play a significant role in producing heavy rains when they are steered out of the Tibetan Plateau (Tao & Ding, 1981). Ding and Chan (2005) showed that strong horizontal wind shear at lower levels or near the surface (Meiyu front) with a weak horizontal temperature gradient is favorable for heavy rainfall. Low-level jets originating in the tropical oceans and embedded in the anticyclonic circulation associated with the Western North Pacific Subtropical High (WNPSH) are closely related to heavy precipitation (G. T. G. Chen et al., 2005, 2006; Sampe & Xie, 2010). Synoptic-scale frontal boundaries accompanied by a trough aloft also facilitate the occurrence of the heavy precipitation (Ding et al., 1980). Although the large-scale background circulations during the Meiyu period have been well documented in previous studies, it is worthwhile to select a recent impactful event and put the latest observations into the context of what is already known, to test and develop the existing theory.

Because of the atmospheric circulation, some MCSs move out of the Tibetan Plateau and affect the downstream areas. In the southwestern part of the Tibetan Plateau, the persistent easterly 500-hPa flow helps the convective cells produced by diurnal heating in the Tibetan Plateau develop into an MCS and move over northern India (Rasmussen & Houze, 2012). Kumar et al. (2014) confirmed the hypothesis of this storm's development in a coupled atmosphere and land surface model, concluding that the effect of the squall line generated by the midlevel jet on the sudden heavy rain event could not be ignored. In the eastern part of the Tibetan Plateau, MCSs driven by a prevailing westerly wind can also affect the downstream Yangtze River Basin. Yasunari and Miwa (2006) found that convective activity over the Tibetan Plateau is closely associated with the downstream heavy precipitation during the Meiyu period. These systems, generated over the Tibetan Plateau, develop into mesoscale cloud systems over the Yangtze River Basin with enhanced latent heating. Such systems are responsible for heavy flooding events in the Yangtze River Basin, as was the case in 1998 (Wang et al., 2019; Yasunari & Miwa, 2006; Zhao et al., 2019). Investigations of the diurnal cycle of summer rain rate over contiguous China have revealed a coherent eastward transition of maximum precipitation from the eastern Tibetan Plateau to the lower Yangtze River Valley (H. Chen et al., 2010; Yu et al., 2007). Hu et al. (2016) identified the Tibetan convective system, finding that 26% of such systems propagate eastward out of the Tibetan Plateau, influencing precipitation over the Tibetan Plateau and its adjacent regions. Therefore, understanding these MCSs and their movement from the Tibetan Plateau can improve forecast accuracy in downstream areas.

The Tibetan Plateau has unique geographic features and lacks traditional ground-based observations. Therefore, research on cloud and precipitation systems in this region relies on satellite and reanalysis data. With the implementation of the Global Precipitation Measurement (GPM) mission in February 2014 and the latest European Centre for Medium-Range Weather Forecasts (ECMWF) reanalysis, ERA5, our ability to study precipitation and atmospheric circulation over the Tibetan Plateau and adjacent regions has improved considerably. Furthermore, the Chinese geostationary satellite, FY-2, can observe brightness temperature at a 30-min temporal resolution. The combination of these three data sources provides us with the opportunity to observe heavy rainfall events that move from the Tibetan Plateau from the aspects of vertical structure and microphysics.

In the summer of 2016, the Yangtze River Basin experienced heavy precipitation, resulting in the worst flooding since 1998. From 29 June to 6 July (UTC was used throughout this paper), the heavy precipitation and associated secondary disasters were responsible for 237 deaths, the disappearance of 93 people, and at least $22 billion in damage (C. Zhou et al., 2018). In particular, the rainfall in Wuhan (one of the nine National Central Cities of China) reached 560.5 mm, breaking the record for the maximum value of weekly continuous precipitation since Wuhan's meteorological records began (China News, from http://www.chinanews.com/sh/2016/07-07/7931215.shtml). Figure 1 shows accumulated precipitation during the eight days from 29 June to 6 July 2016, based on Integrated Multi-satellitE Retrievals for GPM (IMERG). There was a heavy rain belt over the Yangtze River Basin, which extended eastward to the Korean Peninsula. The main body of this rain belt was oriented in the east-west direction, slightly to the northeast-southwest, and its position was similar to the perennial Yangtze-Huai quasi-stationary front during the Meiyu period, which can be considered as a typical summer rain belt caused by the monsoon system. Wuhan experienced two rounds of precipitation during this period. The first was from 30 June to 2 July, and brought rainfall of approximately 150, 97, and 89 mm on each of the three days. The second brought rainfall of approximately 174 mm on 5 July and 40 mm on 6 July.

Although several studies have investigated this event from the perspective of the climate (C. Zhou et al., 2018), flood prevention (Cheng et al., 2018), or high-resolution simulations (P. Li et al., 2019), there are gaps in our understanding of the vertical structure of precipitation and the cloud microphysics.

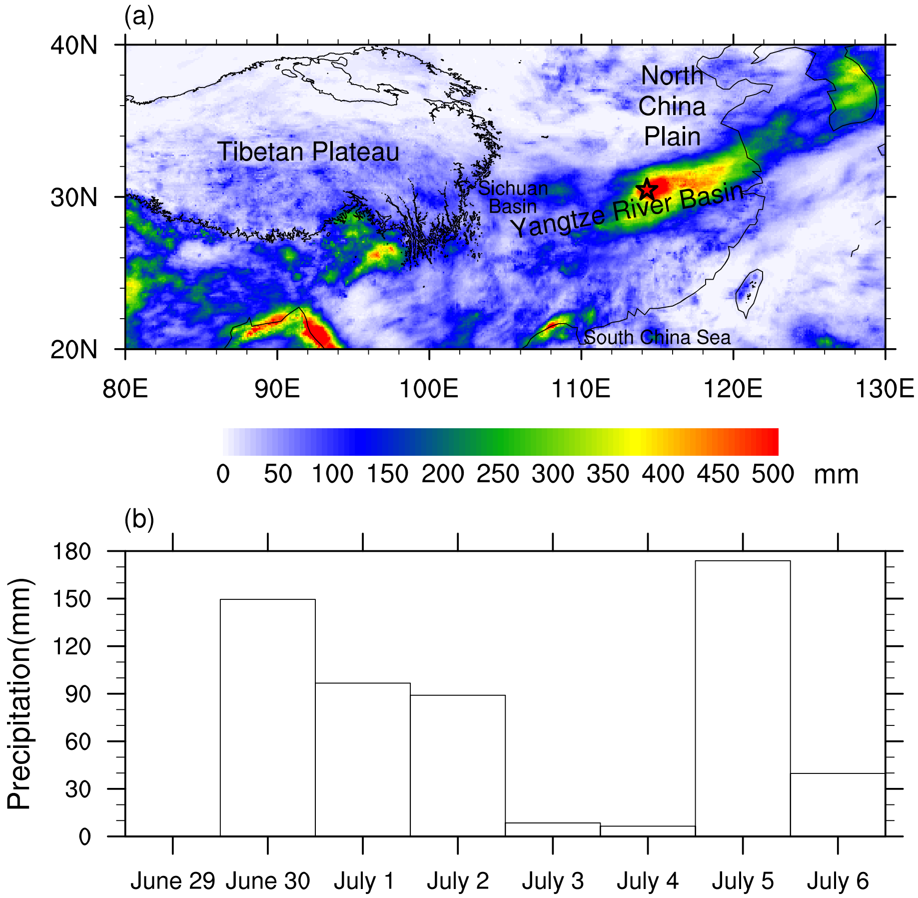

Figure 1. (a) Accumulated precipitation (mm) from 29 June to 6 July 2016 (UTC). The Tibetan Plateau (above 3-km elevation) is denoted by the black solid line. The black pentagram indicates the location of Wuhan. (b) Daily precipitation (mm) in Wuhan, based on data for nearest GPM IMERG point.

Recently, Sun et al. (2020) analyzed near-surface rain, drop size distributions, and vertical structures of Meiyu precipitation systems by classifying them into developing, mature, and dissipating stages, but the effect of the Tibetan Plateau on these parameters is still unknown. This paper focuses on the meteorological triggers and cloud microphysics of this heavy rainfall event in the first stage (the evolution of the heavy rainfall). We believe it would be an impactful case of heavy rainfall in China with the development of observations and reanalysis data, and it is valuable to compare this event with other (typical or atypical) precipitation events during the Meiyu period.

2. Data and Methods

We used GPM IMERG Final Precipitation L3 Half Hourly 0.1° × 0.1° V05 (GPM_3IMERGHH) data to provide rain rate, which uses the differential precipitation-relevant satellite passive microwave sensors in the GPM constellation and is fused to the rain rate estimated by the geostationary infrared (IR) satellite (Huffman et al., 2007). As a "Final" product, the precipitation estimates are adjusted with monthly surface precipitation gauge analysis data. The GPM 2ADPR product is subdivided into DPR_NS (Ku normal scan), DPR_HS (Ka high-sensitivity scan), and DPR_MS (matched scan) products (Iguchi et al., 2012). We used the DPR_NS V08 precipitation product to provide radar reflectivity and droplet size distribution profiles. The droplet size distribution profiles, including those of the mean mass-weighted drop diameter (D_m) and the normalized drop concentration parameter (dBN_w) (Hou et al., 2014), are retrieved by the dual-frequency algorithms at the Ku inner swath and the single-frequency algorithms at the Ku outer swath. The GPM data set is accessible at the National Aeronautics and Space Administration (NASA) Goddard Earth Sciences Data and Information Services Center (https://disc.gsfc.nasa.gov).

ERA5 is the fifth generation of ECMWF atmospheric reanalysis of the global climate and is gradually replacing ERA-Interim as the latest climate reanalysis (Copernicus Climate Change Service (C3S), 2017). This data set is produced using 4D-Var data assimilation and is closely associated with the excellence of the forecast products. Compared with the widely used ERA-Interim, ERA5 makes a number of improvements in the assimilation system, input observations (including precipitation), and has higher temporal and spatial resolutions. The product consists of hourly analysis fields at 31 km on 137 levels, from the surface to 0.01 hPa. The ERA5 data set, covering 1979 to present, is now available for public use. Detailed documentation and download information can be found at the ECMWF website (https://www.ecmwf.int/).

Integrated Global Radiosonde Archive (IGRA) consists of radiosonde and pilot balloon observations at over 2,700 globally distributed stations. It provides observations of pressure, temperature, geopotential height, dew point depression, wind direction, and wind speed at standard levels (Durre et al., 2006). Detailed information of IGRA is accessible via the IGRA webpage (https://www.ncdc.noaa.gov/data-access/weather-balloon/integrated-global-radiosonde-archive).

The FY-2E satellite, which was launched in 2008 and is still in orbit, is the fifth flight unit of the FY-2 series. As a geostationary orbit satellite, it is equipped with a Visible and Infrared Spin Scan Radiometer, which can scan the disk at five bands, including the visible channel (0.5–0.9 μm), midinfrared channel (3.5–4.0 μm), thermal infrared Channel 1 (10.3–11.3 μm), thermal infrared Channel 2 (11.5–12.5 μm), and water vapor channel (6.3–7.6 μm), with a time interval of 30 min. The instrument has a resolution of 1.25 km in the visible channel and 5 km in the infrared channel. The satellite moved from 105°E and replaced FY-2-D as the primary satellite in the 86.5°E position on 1 July 2015. It can now observe cloud-system movements over the Tibetan Plateau and its surroundings. Using the satellite's infrared channel data, several studies have tracked and identified MCSs in China, confirming the data validity (Yang et al., 2015). The data and documentation are accessible at the National Satellite Meteorological Center of the China Meteorological Administration website (http://www.nsmc.org.cn/en/NSMC/Home/Index.html).

Contoured frequency by altitude diagrams (CFADs; Yuter & Houze, 1995a) of reflectivity was used to show the vertical structure of precipitation. The reflectivity of each height layer was interpolated to 0.5 km (vertical resolution) and 1 dBZ (horizontal resolution) intervals. Values were normalized using the overall maximum, so that the value of each bin is distributed between 0% and 100%. Different CFADs were obtained by subtracting the CFAD from different cases. Compared with the normalization-by-level methodology used by McMurdie et al. (2018), normalizing by the overall maximum enables a comparison of values at different height levels (Zagrodnik et al., 2019). In order to mitigate the effect of freezing-level height on CFAD, CFADs were aligned with respect to the height of 0°C (DPR retrievals) before subtraction.

3. Results

During the period from 29 to 30 June, there were two obvious precipitation processes. The first was the southward shift of the East China rain belt on 29 June (Figures 2a–2d). From 0000 to 1800, it moved eastward and then dissipated. The second process was the development of a precipitation system generated in the Tibetan Plateau. A new Meiyu front was established from 1200 on 29 June, while the precipitation system over the Tibetan Plateau moved eastward. Specifically, at 1200 (Figure 2c), precipitation systems gradually developed in the eastern part of the Tibetan Plateau and then began to move southward. At 1800, they arrived at the eastern edge of the Tibetan Plateau and moved off at 0000 on 30 June (Figure 2e), before entering the Sichuan Basin. Thereafter, the precipitation was significantly enhanced, converging into a bigger cluster and continuing to move eastward. From 0600 on 30 June (Figure 2f), the precipitation system gradually moved out of the Sichuan Basin and stretched eastward. At 1200, the precipitation area spread to the Yangtze River Basin and then continued to extend over the sea area. The system connected with the precipitation area to the north, while the precipitation intensity also increased, forming a new Meiyu front belt with a length exceeding 1,000 km.

Next, we examined the circulation and geopotential height at 700 hPa, which are most useful for observing the formation and development of southwest China vortices (SWVs) and low-level jets (Kuo et al., 1988; J. Li et al., 2014). Special attention was paid to the changes in the circulation and geopotential height on the 2 days of our study period, during which an SWV developed.

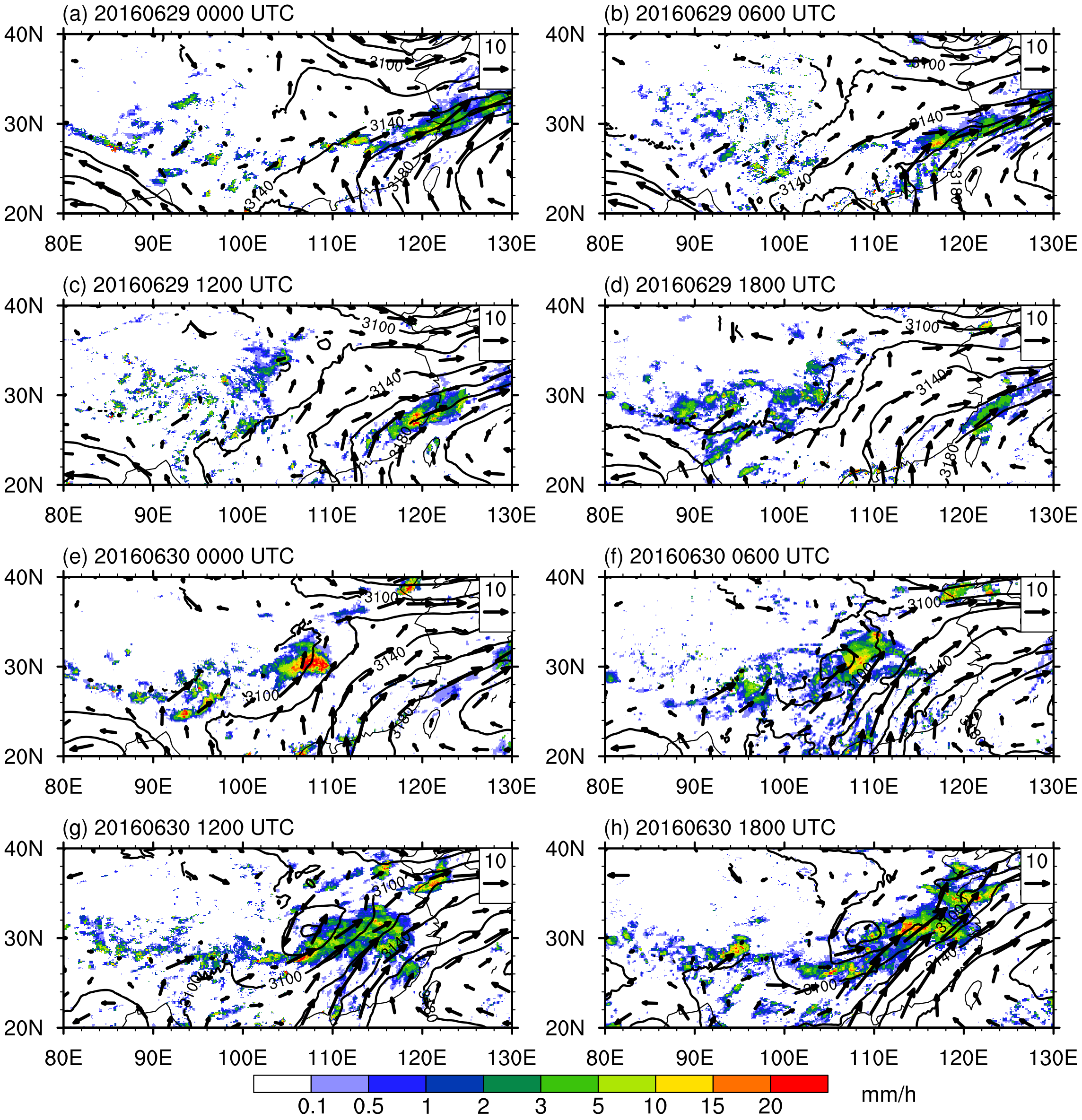

Figure 2. Circulation (vectors) and geopotential height (contours) at 700 hPa at 6-hourly intervals (UTC): (a) 0000 29 June, (b) 0600 29 June, (c) 1200 29 June, (d) 1800 29 June, (e) 0000 30 June, (f) 0600 30 June, (g) 1200 30 June, and (h) 1800 30 June. The shading shows half-hourly rain rate (mm/hr) from GPM IMERG. Since the surface pressure over most of the Tibetan Plateau is less than 700 hPa, the circulation at 700 hPa over the Tibetan Plateau cannot be used for reference.

Before the formation of the SWV, there were strong low-level winds (speeds of 10–15 m/s) along the direction of the parallel isobar of the high-pressure ridge (Figure 2a), which was the reason for the maintenance of the Meiyu front before 29 June. Thereafter, the winds weakened at first (Figures 2b–2d) but then enhanced again as the SWV moved eastward and the low-level jet zone gradually expanded (Figures 2e–2h). Affected by the eastward shift of the SWV, the location of the low-level jet zone was reconstructed, which in turn affected the location of the precipitation zone. Besides, the WNPSH was strong during the eastward movement of the vortex but was weakened and retreating eastward with the development of the vortex. For example, the 3,180-gpm contour retreated five degrees (Figures 2g and 2h) within the 6 hr from 1200 to 1800 on 30 June, and the contour range in the latitudinal direction also greatly shrunk.

The WNPSH is a major circulation system affecting weather and climate in East Asia, and changes in its location, area, and intensity have an important impact on precipitation in China during the flood season (T. Zhou et al., 2009). We used the 500-hPa isobaric data to analyze the formation of the Tibetan Plateau

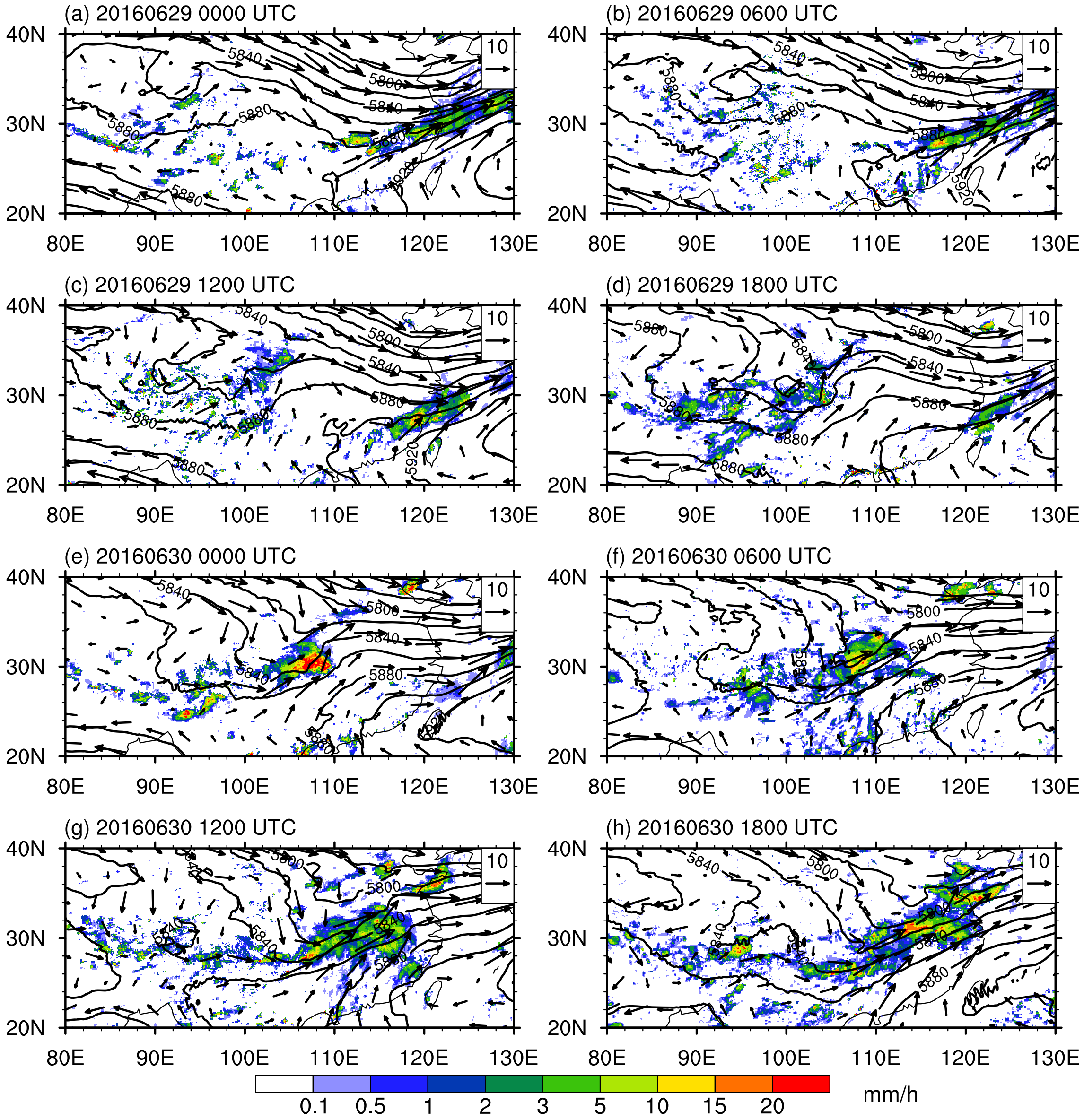

Figure 3. As in Figure 2 but at the 500-hPa level. (a) 0000 29 June, (b) 0600 29 June, (c) 1200 29 June, (d) 1800 29 June, (e) 0000 30 June, (f) 0600 30 June, (g) 1200 30 June, and (h) 1800 30 June.

vortex (TPV) and the activity of the WNPSH. Due to the high altitude of the Tibetan Plateau, however, it is only reliable to data for isobaric levels of 500 hPa or higher to analyze the weather systems that form over the Tibetan Plateau.

From 0000 on 29 June, a vortex began to form in the northern part of the Tibetan Plateau (Figure 3). It continued to deepen over the next 18 hr as it gradually moved eastward. At 0000 on 30 June, the TPV moved out of the Tibetan Plateau and connected to the low pressure zone in the northeast, forming a trough along the eastern edge of the Tibetan Plateau (Figure 3e). The trough subsequently developed and deepened, and the airflow in front of the trough continuously enhanced. The trough continued to move eastward and southward, compressing the WNPSH, as well as the strong horizontal wind shear in the Yangtze River Basin. By 1800 on 30 June, the trough had moved to the North China Plain-Sichuan Basin region (from ~115°E, 35°N to ~106°E, 28°N), with the formation of a strong southwesterly jet over the Yangtze River Basin in front of the trough, and a strong horizontal wind shear line on the northwest side of the jet (Figure 3h).

At 0000 on 29 June (Figure 3a), the 5,880-gpm contour was not closed, and the WNPSH was positioned across the intercepted area. The maximum geopotential height exceeded 5,940 gpm over the west Pacific. After the TPV formed at 0000 on 29 June, the high value center of the WNPSH began to retreat eastward, and the area bounded by the 5,880-gpm contour began to shrink. At 1200 on 29 June, the traversing >5,880-gpm area gradually narrowed and became saddle-shaped (Figure 3c). By 0000 on 30 June, the WNPSH split with the formation of the Tibetan Plateau trough (Figure 3e). Thereafter, the part over the Pacific continued to weaken and retreat eastward. By 1800 on 30 June (Figure 3h), the 5,880-gpm contour had retreated to the southeastern coast of China, and the high value center of the WNPSH had also significantly weakened, though it remained stronger than the climatic mean for the same period (figure omitted). The splitting of the WNPSH led to a large amount of water vapor transport from the southeast to the Yangtze River Basin, providing favorable water vapor conditions for this heavy rainfall event.

Based on the 700-hPa isobaric level data (Figure 2), and according to L. Li et al. (2017), we found that the formation of the TPV was closely related to the formation of the SWV. When the TPV developed and moved out of the Tibetan Plateau, transforming into a Tibetan Plateau trough, a lower SWV gradually formed in the eastern part of the Tibetan Plateau (at 0000 on 30 June). The enhancement of the SWV would also accelerate the low-level jet and produce excessive rainfall (Molinari & Dudek, 1992; D. Zhang et al., 1988). The continuous eastward movement of the SWV influenced the WNPSH, causing it to split and retreat eastward, at the same time generating a strong southwesterly jet. Consequently, low-level water vapor from the South China Sea was transported to the Yangtze River Basin, providing a continuous stream of water vapor for the heavy rains over the next few days.

Xichang station (102.27°E, 27.9°N) is located at the junction of the Tibetan Plateau and the Sichuan Basin and has an elevation of 1,190 m. Therefore, soundings at this site can be used to investigate precipitation formation processes from the perspective of atmospheric stability. Figure 4a shows that at 0000 on 29 June (Figure 4a), it was dry above the 700-hPa level, and the depression of the dew point temperature was 4.2°C at the surface. At 1200 on 29 June, the sounding (Figure 4b) was saturated from 700 to 400 hPa, because the cloud system had begun to move out of the Tibetan Plateau (Figure 5c). However, due to the influence of the WNPSH, low-level water vapor transport had not been established. At this time, there was low convective available potential energy (CAPE), about 420 J/kg. By 0000 on 30 June, the SWV had formed and started to move out from the Sichuan Basin (Figure 2e), the low-level atmosphere was saturated (Figure 4c), there was veering of the wind (warm advection), and CAPE reached 739 J/kg. By 1200 on 30 June, the air was almost completely mixed by prior precipitation, and the thermodynamic profile of the atmosphere appeared saturated and moist neutral (Figure 4d). On the whole, such conditions may trigger moderately embedded convection instead of deep convection (Houze et al., 2017). Stratiform precipitation actually dominated.

The spatial distribution of the infrared brightness temperature observed by FY-2E is shown in Figure 5. It is generally believed that pixels with brightness temperatures lower than 233 K represent regions of ice cloud (Menzel & Strabala, 1997). Large areas of ice clouds usually originate from cloud anvils outside the convective system or are inherently deep convection (Powell et al., 2012). The ice-cloud system in the eastern part of the Tibetan Plateau began to form at 0615 on 29 June (Figure 5b). At 1215, a relatively dense cluster formed, and the cloud mass gradually moved eastward. Meanwhile, the other part of the cloud cluster over the Tibetan Plateau split (Figure 5c). At 1815, the split cluster moved northeastward (~109°E, 35°N), while the major part started to move out of the Tibetan Plateau (Figure 5d). At 0015 on 30 June, the major part moved off the Tibetan Plateau, then continued to develop over the Sichuan Basin (~109°E, 29°N) as it moved eastward (Figure 5e). By 0615, the major system already covered most of the Yangtze River Basin and connected with the newly generated clouds from the southwest (Figure 5f). By this time, the southwesterly jet had already carried low-level water vapor into the system, and the northeast cloud clusters over the sea had gradually developed and accumulated. At 1215, the major cloud system developed vigorously both in size and intensity and began to reshape into a belt shape, stretching itself further over the sea (Figure 5g). By 1815, a cloud belt that traversed the central and eastern parts of China had formed (Figure 5h). It overlapped with the southwesterly jets and continued to develop northeastward.

The life cycle of a cloud cluster consists of a development stage, a mature stage, and a dissipation stage (Byers & Braham, 1949). The minimum brightness temperature first decreases, then hardly changes, and finally continually rises within these stages (Fiolleau & Roca, 2013; A. Zhang & Fu, 2018). There was a relatively

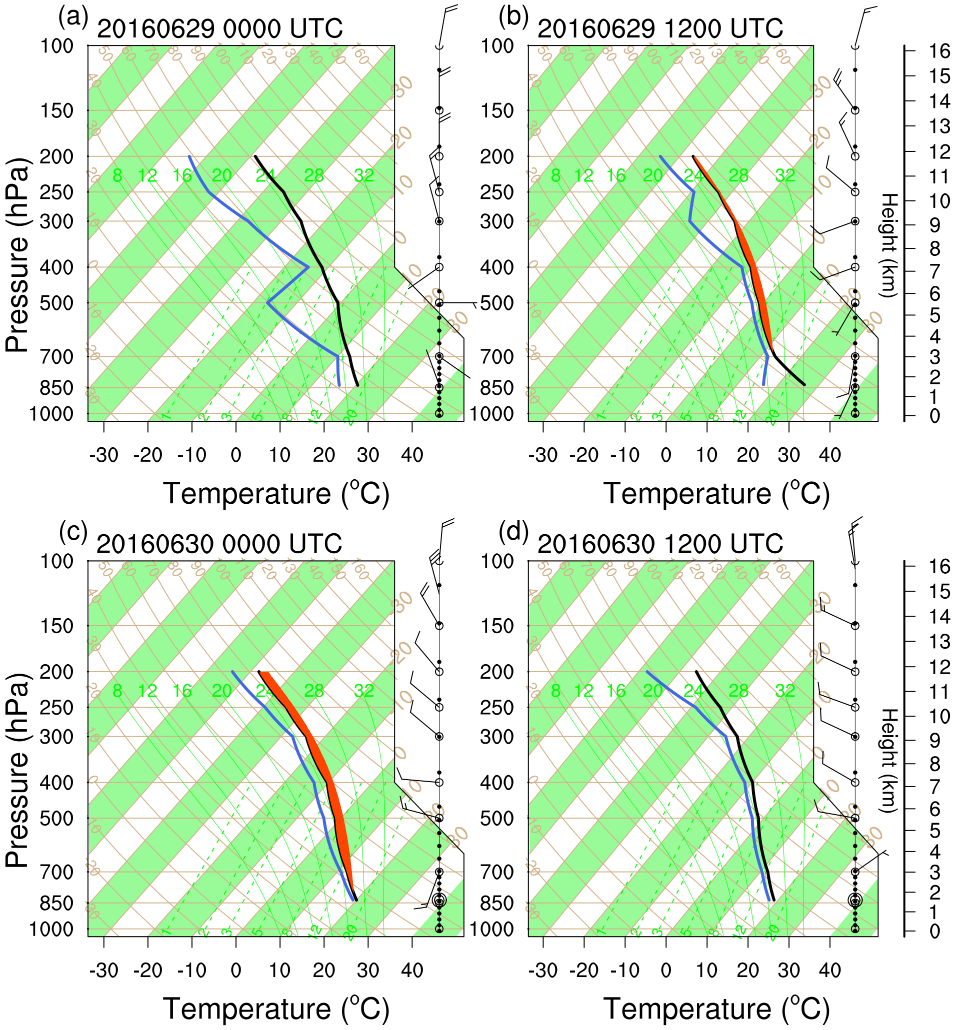

Figure 4. Soundings from Xichang station (102.27°E, 27.9°N) at 12-hr intervals (UTC): (a) 0000 29 June, (b) 1200 29 June, (c) 0000 30 June, and (d) 1200 30 June. The black line and blue line indicate the profiles of temperature and dew point temperature, respectively. The red area indicates the region of CAPE.

obvious "development-mature" process during the eastward movement of this cloud system. Figures 5a–5e (29 June) shows the development of the cloud system, and Figures 5f–5h (0615–1215 on 30 June) shows the mature stage. In the developing stage, the cloud system area did not increase significantly, but the minimum brightness temperature had reduced sharply. For instance, at 0015 on 30 June, a compact low brightness temperature cell (<213 K) appeared in the eastern part of the Sichuan Basin (~109°E, 29°N), which may have occurred because of tropopause-penetrating convection. In the mature stage, the coverage of ice cloud increased, developing into a large cloud system that covered the whole of southern China, and forming and maintaining a new Meiyu front rain belt (Figure 5h).

During the eastward movement of the cloud system from 29 to 30 June, the GPM Dual-frequency Precipitation Radar (DPR) scanned twice, both behind the trough at 500 hPa located at the trailing part of the cloud system (Figures 6a and 6b). Considering the relative position (with trough and with cloud cluster), wind speed, northwest wind, and continuously observations of brightness temperature (FY-2E) and rain rate (GPM IMERG), the latter case (Case 2) developed from the movement of the earlier case (Case 1). The brightness temperatures in the DPR scanning regions were lower than 253 K in both cases, while the latter case also involved deep cloud with a brightness temperature lower than 213 K. This means that ice-phase processes (including deposition, riming, and melting) and warm-phase processes (including condensation, coalescence, and evaporation) may have coexisted in the two cases. An in-depth study of the two cases can help

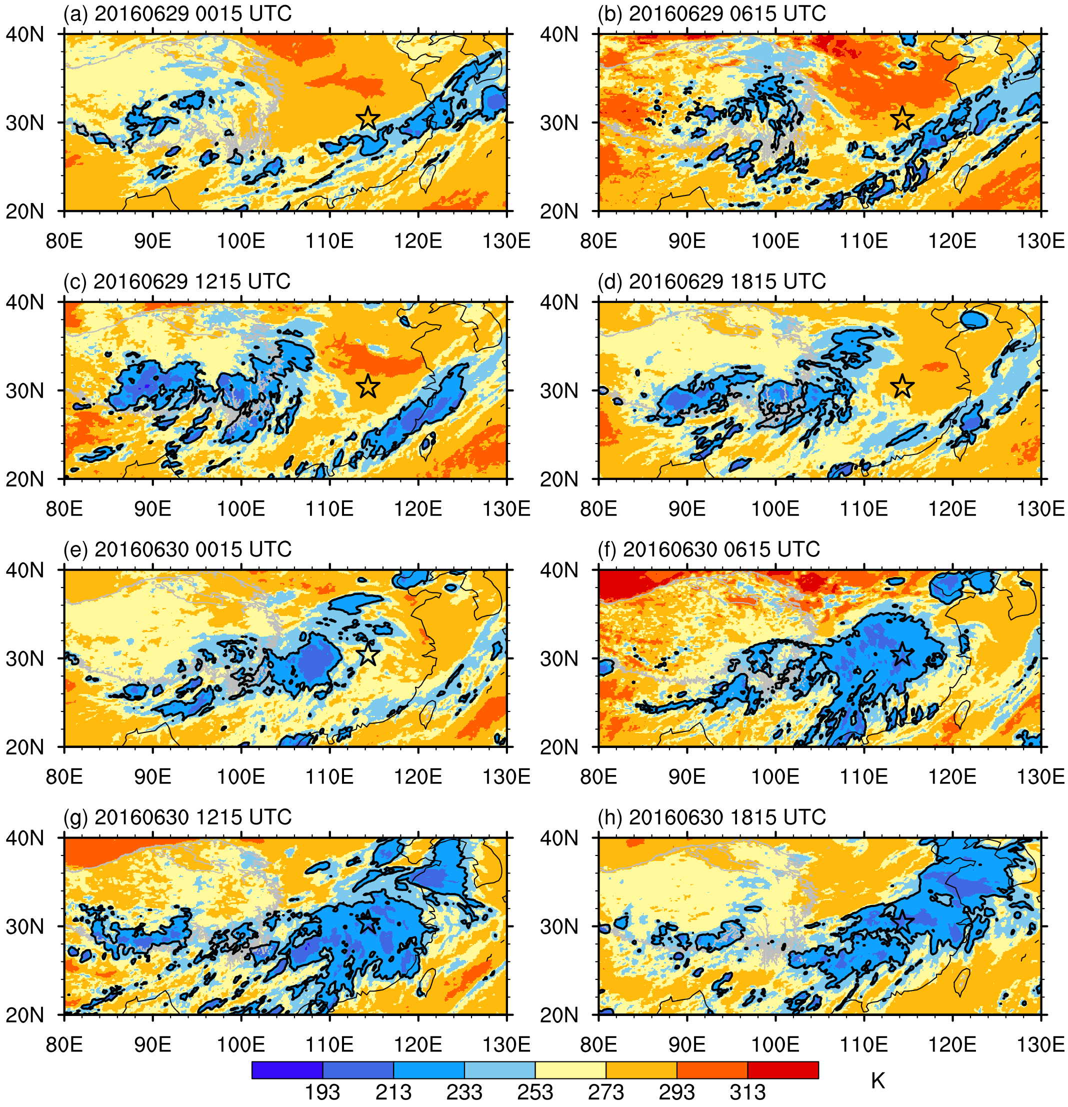

Figure 5. The brightness temperature observed by the FY-2E thermal infrared channel 1 (10.3–11.3 μm). (a) 0015 29 June, (b) 0615 29 June, (c) 1215 29 June, (d) 1815 29 June, (e) 0015 30 June, (f) 0615 30 June, (g) 1215 30 June, and (h) 1815 30 June. Blue shading bounded by black lines indicates brightness temperature values lower than 233 K. The black pentagram indicates the location of Wuhan. The Tibetan Plateau (above 3-km elevation) is denoted by the gray solid line.

reveal the detailed vertical structure and microphysical process of the precipitation system as it moved out of the Tibetan Plateau. According to ERA5 reanalysis (Figures 6c and 6e), the vertical integral of water vapor flux in the heavy precipitation area of Case 2 exceeded 250 kg m^{-1} s^{-1}, whereas the values in Case 1 were less than 200 kg m^{-1} s^{-1}. Case 2 shows a greater negative value of vertically integrated moisture divergence (-6×10^{-4} kg m^{-2} s^{-1}) than Case 1, favoring the development of cloud and precipitation. This indicates that the water vapor supply in Case 2 was stronger than that in Case 1. Precipitation in Case 1 was still located over the Tibetan Plateau, with an average elevation of 4 km (Figure 6e). Precipitation in Case 2 was located at the junction of the Tibetan Plateau and the Sichuan Basin, and the elevation was distributed between 1.5 and 3.5 km (Figure 6f). Precipitation in Case 1 was generally weak, with a rain rate of less than 4 mm/hr. Although Case 2 also involved a large area with a weak rain rate, there was a heavy precipitation area in the south of the precipitation system (between 27°N and 28°N), with a rain rate above 20 mm/hr.

The cross sections along the AB line (Figure 6e) and CD line (Figure 6f) of the GPM DPR scans are shown in Figure 7. The reflectivity values in the AB section were generally weak, below 30 dBZ, and the bright band

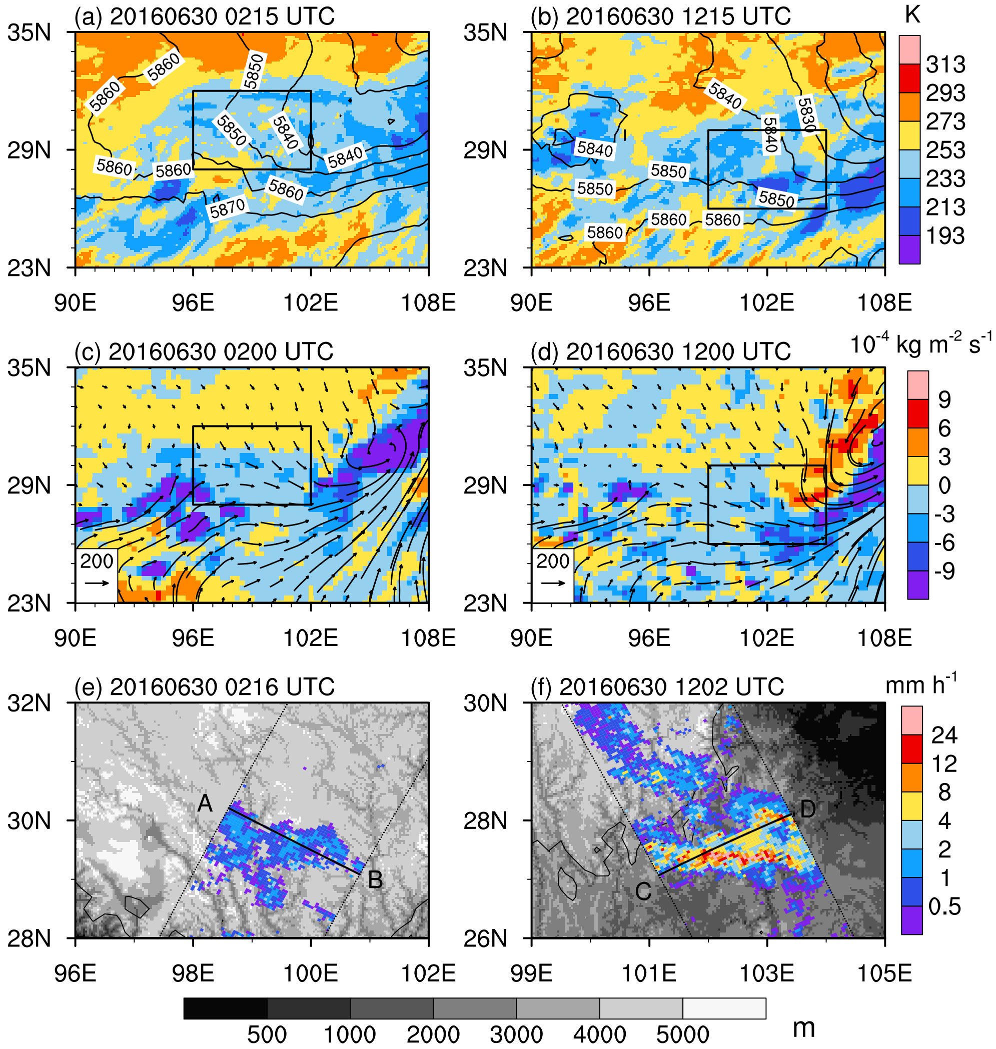

Figure 6. Spatial distributions of (a, b) 500-hPa geopotential height (contours) and brightness temperature of the thermal infrared channel (shading), (c, d) vertical integral of water vapor flux (vectors) and mean vertically integrated moisture divergence (shading), and (e, f) near-surface rain rate (colored shading) and elevation (grayscale shading) for precipitation systems over the Tibetan Plateau (left panels) and at the junction of the Tibetan Plateau and the Sichuan Basin (right panels). The Tibetan Plateau (above 3-km elevation) is denoted by the black solid line.

was not obvious. However, the echo-top height was not shallow (~8 km) and in fact reached 10 km (Figure 7a). The freezing level was only 1 km higher than the land surface, and therefore, there was not enough space for warm-phase process. Ice-phase processes may have been the dominant microphysical mechanisms in this case. The reflectivity of the CD section showed completely different characteristics from that of AB section. There was an obvious convective cell at ~95 km (Figure 7b), which was accompanied by strong upward movement and dominated by the collision-coalescence process. At the same time, it also acted as a "particle fountain" (Yuter & Houze, 1995b), carrying the lighter particles upward and transporting them to the surrounding areas and accelerating the growth of the surrounding precipitation particles. For example, Figure 7d shows that the droplet concentration was higher near ~95 and ~230 km than in other regions. Between convective cells, there was a clear bright band, which showed stratiform precipitation characteristics, and riming (aggregation) was the dominant mechanism for this structure. There were also differences in D_m values on the AB and CD sections. On the AB section, D_m varied little with distance, between 1 and 1.4 mm, and only slightly increased with decreasing height in the vertical direction (Figure 7e). This feature implies that collection (including coalescence, riming, and aggregation) is not the dominant mechanism of precipitation over the Tibetan Plateau. In

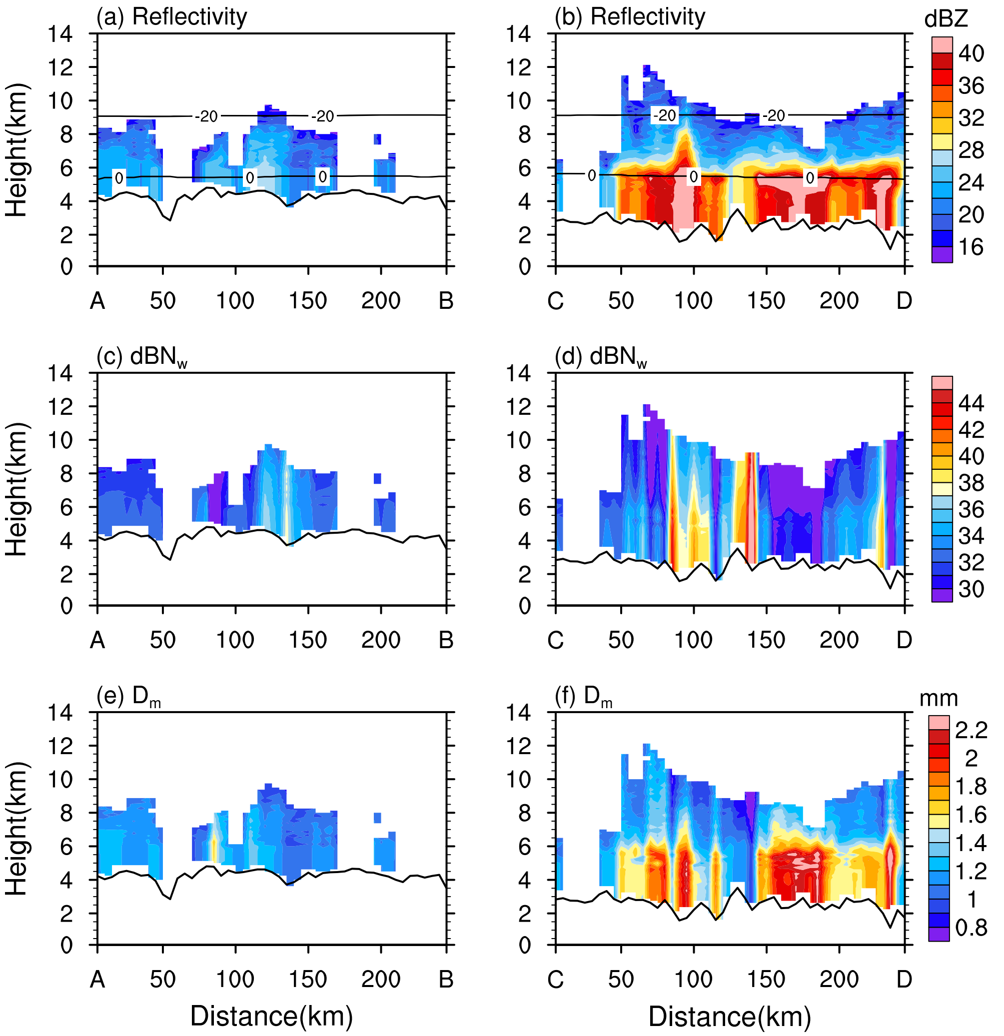

Figure 7. Vertical cross sections (AB in Figure 6e and CD in Figure 6f) of (a, b) the attenuation-corrected Ku band reflectivity, (c, d) the normalized drop concentration parameter (dBN$_W$), and (e, f) the mean mass-weighted drop diameter (D$_m$) for precipitation systems over the Tibetan Plateau (left panels) and at the junction of the Tibetan Plateau and the Sichuan Basin (right panels). Key temperature levels (0°C and −20°C) are overlaid on (a) and (b) from the ERA5 reanalysis.

contrast, on the CD section (such as 150–200 km), D$_m$ was greater than 2 mm (Figure 7f), which indicates that there was a strong particle growth mechanism (aggregation) near the freezing level (Houze, 1997).

The CFADs were calculated from all the data shown in Figure 6e (Case 1) and Figure 6f (Case 2). In both Case 1 and Case 2, the 50% contour line decreased almost linearly from ~23 dBZ at 5 km to ~18 dBZ at 8 km (Figures 8a and 8b). The outlier contours (10% and 30%) and modal contours (70% and 90%) of Case 1 showed almost the same characteristics, indicating uniform vertical structure and microphysics (weak stratiform precipitation). The outlier contours of Case 2 showed markedly different characteristics from Case 1. The reflectivity distribution was much wider, indicating a more diverse droplet size distribution and microphysical processes. In terms of altitude, some contours of Case 2 exceed 10 km. Between 5 and 7 km, the slope of the outer contours changed abruptly, and the maximum reflectivity of the 30% (10%) contour reached 34 dBZ (42 dBZ) near the freezing level. Figure 8c shows that Case 1 and Case 2 mainly differ in the weak echo area of the upper layer and the strong echo area near the freezing level. The rapid increase of echoes 1–2 km above the freezing layer lead to an increase in echoes of subsequent low level.

Figures 9a and 9b show the sample size distributions of the near-surface D$_m$ and dBN$_w$ in the two cases, respectively. By calculating the cumulative precipitation contribution of each bin for the two precipitation

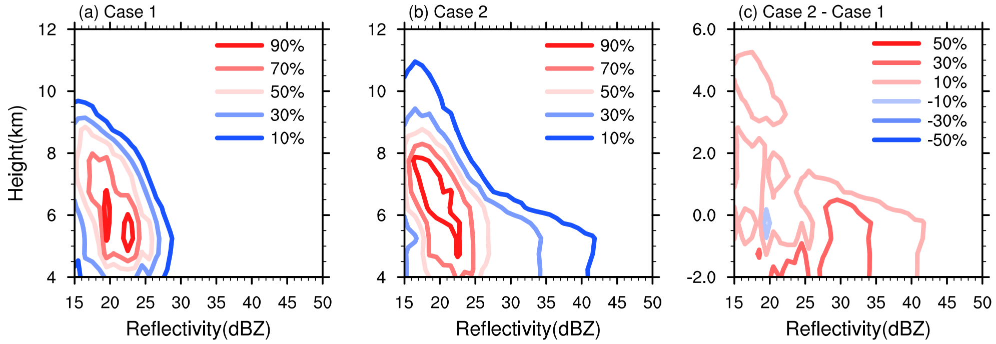

Figure 8. Normalized CFADs of GPM DPR reflectivity for (a) Case 1, (b) Case 2, and (c) Case 2-Case 1. CFADs are aligned with respect to the height of 0°C before subtraction. The 0 km in (c) indicates the height of 0°C.

cases, the difference between the cumulative precipitation contributions of the two cases was calculated (Figure 9c), to assess which D_m and dBN_w configuration contributed the most precipitation. The two cases have similar modes, with dBN_w between 30 and 36, and D_m between 0.8 and 1.6 mm. The difference between the two cases was that the distribution in Case 2 is wider. Figure 9c shows that a slightly greater dBN_w with a slightly larger D_m contributed the most precipitation in Case 2; greater dBN_w was the second largest contribution, and larger D_m contributed less than 5% of the cumulative precipitation. Zagrodnik et al. (2018) found that over the Olympic Mountains, modest precipitation enhancement (deep stratiform cloud) occurs with moderate D_m and dBN_w, and that large numbers of small particles (greater dBN_w) are prone to collide and coalesce to form strong convective precipitation. This theory is in good agreement with the results shown in Figure 9c. Although the number of high dBN_w samples was small (Figure 9b), these samples were associated with more precipitation than other bins with similar sample numbers.

The particles in the ice phase and water phase have different characteristics, and comparing them directly may introduce additional errors. It is necessary to separate them according to the phase before making a comparison at all the levels (Figure 10), which indicates the overall difference of dBN_w-D_m configuration between the ice-phase and water-phase processes. Precipitation phases were discriminated by DPR retrievals. Case 2 had a small amount (~1%) of particles with great dBN_w (>42) and small D_m (<1.0 mm) compared to Case 1 in the ice phase (Figures 10a and 10b), which confirms the "particle fountain" described earlier. For the regime of moderate droplet size distributions ($28 < dBN_w < 42$, $0.8\ mm < D_m < 2.2\ mm$), D_m in Case 2 was overall larger than that in Case 1, indicating the difference in ice-phase processes. From the ice phase to the water phase, Case1 had almost no change (Figure 10c), while droplet size distributions in Case 2 continued to increase in the direction of great dBN_w and large D_m (Figure 10d).

To further reveal the details of the physical process in this event, Figure 11 shows the mean profiles of the droplet size distributions and the vertical velocity for the two cases. In-depth analysis of the profiles can

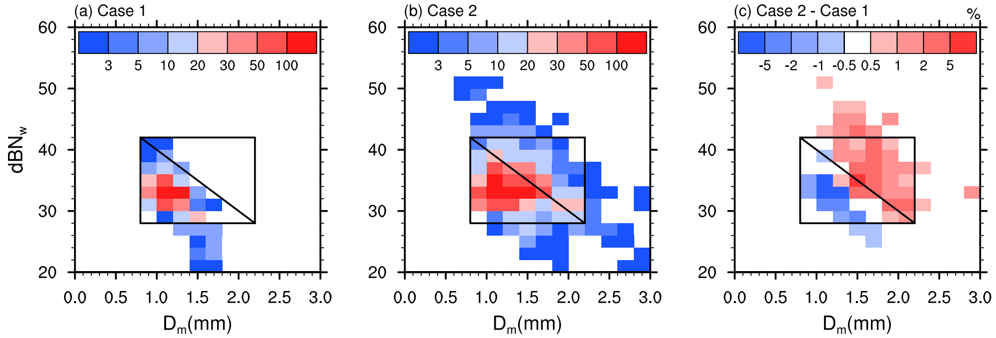

Figure 9. Two-dimensional histograms of near-surface droplet size distributions for sample sizes in (a) Case 1, (b) Case 2, and (c) the difference between the cumulative precipitation contributions of the two cases for each bin. The rectangles donate the regime of moderate droplet size distributions ($28 < dBN_w < 42$, $0.8\ mm < D_m < 2.2\ mm$).

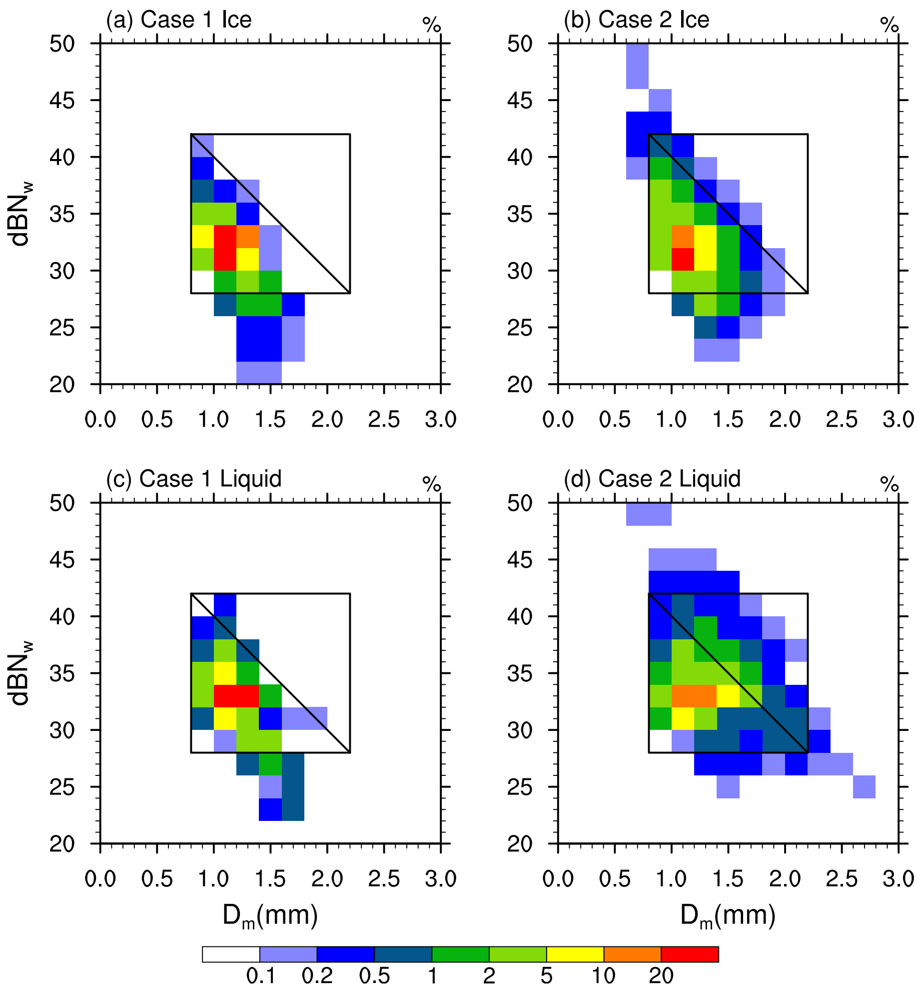

Figure 10. Two-dimensional histograms of droplet size distributions with (a, b) ice phase and (c, d) liquid phase at all the height levels. The rectangles donate the regime of moderate droplet size distributions ($28 < \mathrm{dBN_w} < 42$, $0.8\ \mathrm{mm} < D_m < 2.2\ \mathrm{mm}$).

reveal the subtle changes in droplet size distributions with height. The vertical velocity was derived from the ERA5 reanalysis. We matched the nearest ERA5 grid to each DPR precipitation pixel and then obtained the average vertical velocity profile. $\mathrm{dBN_w}$ in Case 2 was greater than that in Case 1 throughout the profile. The difference between the two reached its maximum near the freezing level. The difference at the levels <5 km was greater than the difference at levels >7 km. This is because Case 2 was affected

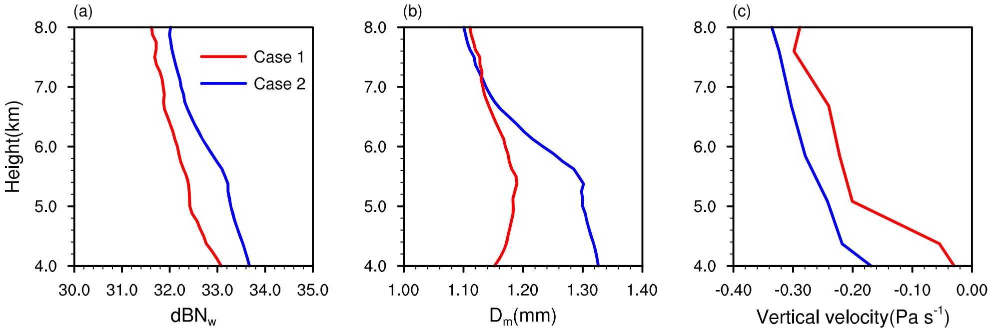

Figure 11. Regional mean profiles of (a) $\mathrm{dBN_w}$, (b) D_m, and (c) vertical velocity in Case 1 (red lines) and Case 2 (blue lines).

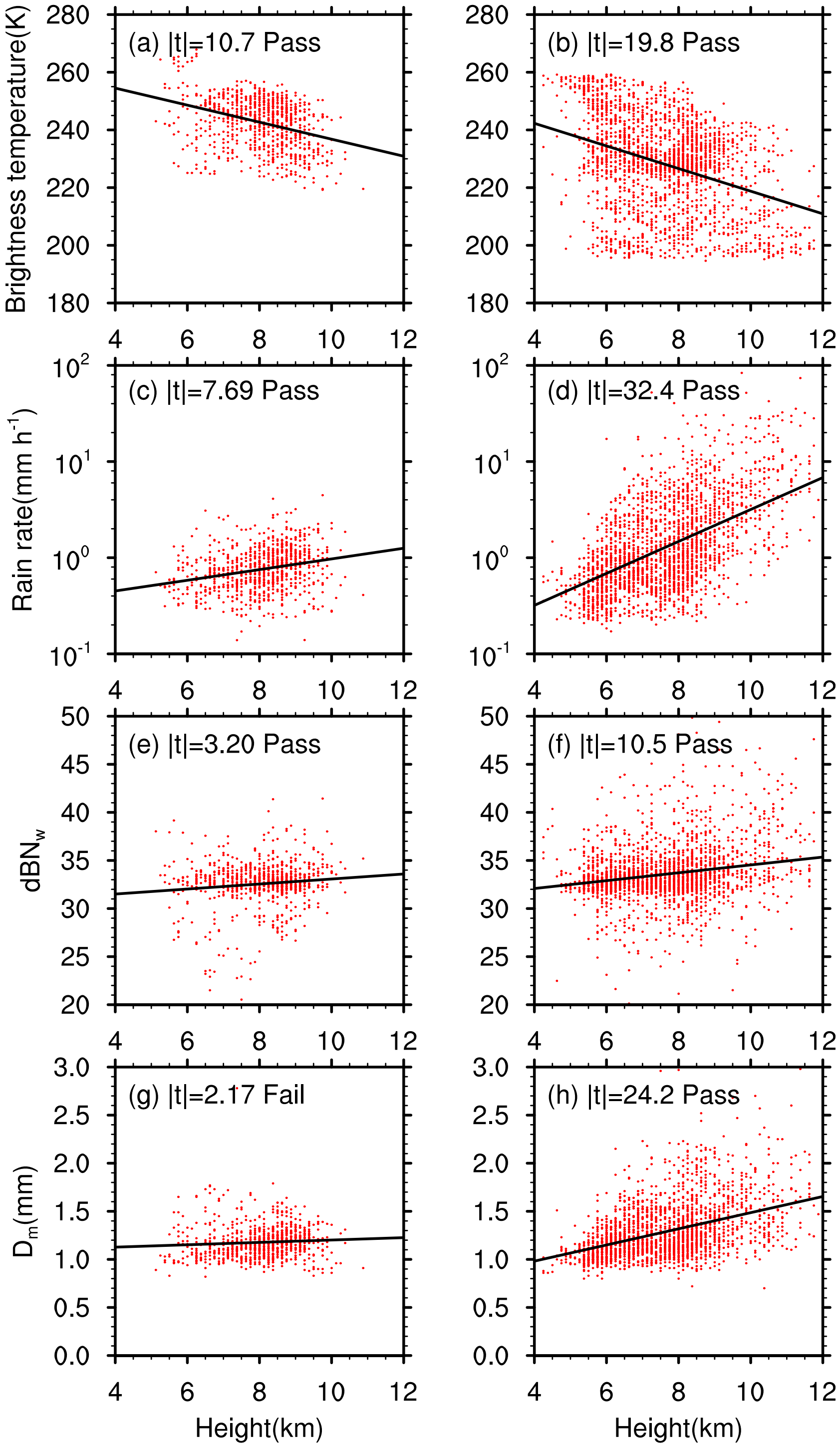

Figure 12. Scatterplots of storm-top height against (a, b) brightness temperature of the thermal infrared channel, (c, d) near-surface rain rate, (e, f) near-surface dBN_w, and (g, h) near-surface D_m for Case 1 (left panels) and Case 2 (right panels), |*t*| is the *t* score of Student's *T* tests, and the significance level is set to 99%. The black lines donate the regression lines.

by the southwesterly airflow, which brought more particles, and the light particles were lifted higher by the upward movement. The shape of dBN_w profile in Case 2 is similar to those of stratiform precipitation over the eastern China (A. Zhang & Fu, 2018) and central China (Sun et al., 2020), while dBN_w profile in Case 1 shows many differences with them.

The vertical structure of D_m (Figure 11b) shows interesting results. In both cases, D_m decreased slightly (and at the same rate) as height increases above 7 km (~2 km higher than freezing level), which indicates that the deposition process of the two cases was almost the same here. Between 7 and 5.5 km in Case 1, D_m continued to increase linearly with decreasing height, whereas in Case 2 the increase was faster; D_m increased from 1.14 mm at 7 km to 1.3 mm at 5.5 km, indicating relatively stronger riming and aggregation during the falling of ice particles. In Case 1, D_m decreased with decreasing height below the freezing level, which may be due to evaporation after raindrops leave the cloud, while D_m in Case 2 increased with decreasing height, which indicates the existence of a collision-coalescence process. The decreasing D_m in Case 1 is somewhat rare in previous study. Even in the dissipating stage with weakest precipitation, the D_m profile is constant below the freezing level over the central China (Sun et al., 2020). The development of convection in Case 2 is the reason that there are more samples with larger D_m in Figure 10b than those in Figure 10a, which is probably because of more graupels exist in Case 2 due to stronger riming processes. Although the presence of a warm-phase process at the levels <5 km was evident in Case 2, the ice-phase process dominated the increase in particle size. The vertical distribution of the vertical velocity shows that in the layer where D_m was rapidly increasing (5.5–7 km), the ascent was moderate (-0.25 to -0.3 Pa s^{-1}), which is conducive to the lifting of ice particles, therefore extending the time for riming and aggregation. Below 5 km, the ascending speed was weakened, which does not favor the occurrence of the warm-phase process.

At last, we carried out a correlation analysis of echo-top height with brightness temperature, near-surface rain rate and near-surface droplet size distributions of the two cases (Figure 12). The echo-top height is the maximum height that the precipitation particles can reach, which represents the depth of precipitation development and is closely related to particle growth. For the same echo-top height, the brightness temperature in Case 1 was ~10 K higher than that in Case 2 (Figure 12a and 12b), which indicates a smaller distance between cloud top and rain top over the Tibetan Plateau. This finding is consistent with Luo et al. (2011), while the slopes in Figures 12a and 12b also show that the brightness temperature in Case 2 decreased faster as the rain top increased. Near-surface rain rate increased with the increasing echo-top height, while the increasing rate was greater in Case 2 (Figures 12c and 12d). As suggested by Yan et al. (2016), the plateau topography causes suppression effect on the precipitation intensity. Here, the difference in microphysics should be also taken into account.

It is surprising that near-surface dBN_w shows similar slope between two cases, while the value in Case 2 was overall greater (Figures 12e and 12f). Large quantities of drops are usually in areas with strong horizontal vapor transport (Zagrodnik et al., 2019), but they may only have a little effect on the echo-top height. Although deep precipitating clouds (echo top > 8 km) existed over the Tibetan Plateau, their D_m remained consistent (Figure 12g), meaning the lack of ice-phase growth. Deep precipitating clouds in Case 2 showed considerable growth of D_m (from ~1.0 mm at 4 km to ~1.5 mm at 10 km) (Figure 12h), resulting a modest precipitation enhancement (stratiform) as the system moved out of the Tibetan Plateau.

4. Conclusions and Discussions

By combining satellite observations, soundings, and reanalysis data, we have investigated the meteorological triggers and cloud microphysics of a heavy rainfall event over the Yangtze River Basin in 2016. In contrast to previous studies of this heavy rainfall event, which were from the perspective of climate (C. Zhou et al., 2018), flood prevention (Cheng et al., 2018), high-resolution simulations (P. Li et al., 2019), and life stage of Meiyu precipitation (Sun et al., 2020), we have focused on observations of the precipitation vertical structure and droplet size distributions before and after the system moving out of the Tibetan Plateau, which are essential for the realistic simulation of such events (D. Zhang et al., 1994). The main conclusions of this work are as follows.

1. The initiating factor for this heavy precipitation event was the generation and eastward movement of a cloud system from the Tibetan Plateau. It moved eastward under the influence of the prevailing westerlies, gradually forming a new frontal rain band. The WNPSH produced low-level jets at 700 hPa and provided sufficient water vapor and momentum for the formation of heavy precipitation.
2. Near-surface precipitation particles got larger and denser with the eastward movement of the cloud system. Slightly larger and slightly denser particles (enhancement of stratiform precipitation) contributed

the most precipitation, while denser and smaller particles (trigger of convective cells) contributed the second largest contribution.

3. As the cloud system moved out of the Tibetan Plateau, the vertical structure of precipitation changed significantly below 7 km. The riming and aggregation processes were significantly enhanced, whereas the deposition process remained the same. Convective cells were triggered, corresponding to high reflectivity. Although the presence of a warm-phase process was evident, the riming and aggregation process between 7 and 5.5 km dominated the increase in particle size.
4. The rain top over the Tibetan Plateau was more packed, and the rain rate increased slower with the increase of echo-top height. After the cloud system moved out of the Tibetan Plateau, the increased echo-top height had a considerable positive impact on near-surface particle size, while this trend was not significant over the Tibetan Plateau.

Considering the cloud system movement at the middle to high levels, the low-level water vapor transport, and the changes in the precipitation vertical structure, the mode of precipitation enhancement of this event can be summarized as "seeder-feeder," although this mechanism is usually used to explain air flowing up and over a hill or small mountain (Houze, 2012). The microphysics of this event was dominated by the combination of the eastward moving cloud system, acting as continuous "seeder" cloud, with the increasing water vapor that enhanced the "feeder" cloud. The particles from the "seeder" cloud grew by the lower "feeder" cloud, thus increasing the particle size to enhance the precipitation.

Data Availability Statement

The GPM_3IMERGHH and GPM 2ADPR data files used in this study are publicly available from the website (https://disc.gsfc.nasa.gov/datasets?keywords=GPM%page=1). The ERA5 data files used in this study are publicly available from the website (https://cds.climate.copernicus.eu/cdsapp#!/dataset/reanalysis-era5-pressure-levels). The FY-2E data files used in this study are publicly available from the http://fy4.nsmc.org.cn/portal/en/theme/FY4A.html website. The IGRA data files used in this study are publicly available from the website (https://www.ncdc.noaa.gov/data-access/weather-balloon/integrated-global-radiosonde-archive).

Acknowledgments

This research was supported by NSFC Project under Grants 91837310, 91637211, and 41620104009; the National Key R&D Program of China under Grants 2017YFC1501402 and 2018YFC1507200; and the Key research and development projects in Anhui province under Grant 201904a07020099.

References

Barros, A. P., Kim, G., Williams, E., & Nesbitt, S. W. (2004). Probing orographic controls in the Himalayas during the monsoon using satellite imagery. *Natural Hazards and Earth System Sciences*, *4*(1), 29–51. https://doi.org/10.5194/nhess-4-29-2004

Byers, H. R., & Braham, R. R. (1949). *The thunderstorm: Report of the thunderstorm project*. Washington, DC: U.S. Government Printing Office.

Chen, G. T. J., Wang, C. C., & Lin, D. T. W. (2005). Characteristics of low-level jets over northern Taiwan in mei-yu season and their relationship to heavy rain events. *Monthly Weather Review*, *133*(1), 20–43. https://doi.org/10.1175/MWR-2813.1

Chen, G. T. J., Wang, C. C., & Lin, L. F. (2006). A diagnostic study of a retreating mei-yu front and the accompanying low-level jet formation and intensification. *Monthly Weather Review*, *134*(3), 874–896. https://doi.org/10.1175/MWR3099.1

Chen, H., Yu, R., Li, J., Yuan, W., & Zhou, T. (2010). Why nocturnal long-duration rainfall presents an eastward-delayed diurnal phase of rainfall down the Yangtze River valley. *Journal of Climate*, *23*(4), 905–917. https://doi.org/10.1175/2009JCLI3187.1

Chen, Y., Fu, Y., Xian, T., & Pan, X. (2017). Characteristics of cloud cluster over the steep southern slopes of the Himalayas observed by CloudSat. *International Journal of Climatology*, *37*(11), 4043–4052. https://doi.org/10.1002/joc.4992

Cheng, X., Wan, H., Huang, S., Li, C., & Zhang, H. (2018). Lessons learned from the 2016 Yangtze River flood in Anhui province, China. *International Journal of River Basin Management*, *16*(3), 307–314. https://doi.org/10.1080/15715124.2018.1437741

Copernicus Climate Change Service (C3S) (2017). ERA5: Fifth generation of ECMWF atmospheric reanalyses of the global climate. Copernicus Climate Change Service Climate Data Store (CDS), date of access. https://cds.climate.copernicus.eu/cdsapp#!/home

Ding, Y. (1992). Summer monsoon rainfalls in China. *Journal of the Meteorological Society of Japan*, *70*(1B), 373–396. https://doi.org/10.2151/jmsj1965.70.1B_373

Ding, Y., & Chan, J. C. L. (2005). The East Asian summer monsoon: An overview. *Meteorology and Atmospheric Physics*, *89*(1-4), 117–142. https://doi.org/10.1007/s00703-005-0125-z

Ding, Y., Li, H., Cai, Z., & Li, J. (1980). On the physical conditions of occurrence of heavy rainfall and severe convective weather. Proc. Eighth Conf. on Weather Forecasting and Analysis, Denver, CO, American Meteorological Society, 371–377.

Durre, I., Vose, R. S., & Wuertz, D. B. (2006). Overview of the Integrated Global Radiosonde Archive. *Journal of Climate*, *19*(1), 53–68. https://doi.org/10.1175/JCLI3594.1

Fiolleau, T., & Roca, R. (2013). An algorithm for the detection and tracking of tropical mesoscale convective systems using infrared images from geostationary satellite. *IEEE Transactions on Geoscience and Remote Sensing*, *51*(7), 4302–4315. https://doi.org/10.1109/TGRS.2012.2227762

Fu, Y., Liu, G., Wu, G., Yu, R., Xu, Y., Wang, Y., et al. (2006). Tower mast of precipitation over the central Tibetan Plateau summer. *Geophysical Research Letters*, *33*, L05802. https://doi.org/10.1029/2005GL024713

Fu, Y., Ma, Y., Zhong, L., Yang, Y., Guo, X., Wang, C., et al. (2020). Land surface processes and summer cloud-precipitation characteristics in the Tibetan Plateau and their effects on downstream weather: A review and perspective. *National Science Review*, *7*(3), 500–515. https://doi.org/10.1093/nsr/nwz226

Fu, Y., Pan, X., Xian, T., Liu, G., Zhong, L., Liu, Q., et al. (2018). Precipitation characteristics over the steep slope of the Himalayas in rainy season observed by TRMM PR and VIRS. *Climate Dynamics*, *51*(5–6), 1971–1989. https://doi.org/10.1007/s00382-017-3992-3

Hou, A. Y., Kakar, R. K., Neeck, S., Azarbarzin, A. A., Kummerow, C. D., Kojima, M., et al. (2014). The Global Precipitation Measurement mission. *Bulletin of the American Meteorological Society*, *95*(5), 701–722. https://doi.org/10.1175/BAMS-D-13-00164.1

Houze, R. A. (1997). Stratiform precipitation in regions of convection: A meteorological paradox? *Bulletin of the American Meteorological Society*, *78*(10), 2179–2196. https://doi.org/10.1175/1520-0477(1997)078%3C2179:SPIROC%3E2.0.CO;2

Houze, R. A. (2004). Mesoscale convective systems. *Reviews of Geophysics*, *42*, RG4003. https://doi.org/10.1029/2004RG000150

Houze, R. A. (2012). Orographic effects on precipitating clouds. *Reviews of Geophysics*, *50*, RG1001. https://doi.org/10.1029/2011RG000365

Houze, R. A., Mcmurdie, L. A., Rasmussen, K. L., Kumar, A., & Chaplin, M. M. (2017). Multiscale aspects of the storm producing the June 2013 flooding in Uttarakhand, India. *Monthly Weather Review*, *145*(11), 4447–4466. https://doi.org/10.1175/MWR-D-17-0004.1

Houze, R. A., Wilton, D. C., & Smull, B. F. (2007). Monsoon convection in the Himalayan region as seen by the TRMM precipitation radar. *Quarterly Journal of the Royal Meteorological Society*, *133*, 1389–1411. https://doi.org/10.1002/qj.106

Hu, L., Deng, D., Gao, S., & Xu, X. (2016). The seasonal variation of Tibetan Convective Systems: Satellite observation. *Journal of Geophysical Research: Atmospheres*, *121*, 5512–5525. https://doi.org/10.1002/2015JD024390

Huffman, G. J., Bolvin, D. T., Nelkin, E. J., Wolff, D. B., Adler, R. F., Gu, G., et al. (2007). The TRMM multisatellite precipitation analysis (TMPA): Quasi-global, multiyear, combined-sensor precipitation estimates at fine scales. *Journal of Hydrometeorology*, *8*(1), 38–55. https://doi.org/10.1175/JHM560.1

Iguchi, T., Seto, S., Meneghini, R., Yoshida, N., Awaka, J., Kubota, T., et al. (2012). An overview of the precipitation retrieval algorithm for the Dual-frequency Precipitation Radar (DPR) on the Global Precipitation Measurement (GPM) mission's core satellite. Earth Observing Missions and Sensors: Development, Implementation, and Characterization II, International Society for Optics and Photonics, 8528, 85281C. https://doi.org/10.1117/12.977352

Kumar, A., Houze, R. A., Rasmussen, K. L., & Peters-Lidard, C. (2014). Simulation of a flash flooding storm at the steep edge of the Himalayas. *Journal of Hydrometeorology*, *15*(1), 212–228. https://doi.org/10.1175/JHM-D-12-0155.1

Kuo, Y. H., Cheng, L. S., & Bao, J. W. (1988). Numerical-simulation of the 1981 Sichuan flood.1. Evolution of a mesoscale southwest vortex. *Monthly Weather Review*, *116*(12), 2481–2504. https://doi.org/10.1175/1520-0493(1988)116%3C2481:NSOTSF%3E2.0.CO;2

Li, J., Du, J., Zhang, D., Cui, C., & Liao, Y. (2014). Ensemble-based analysis and sensitivity of mesoscale forecasts of a vortex over Southwest China. *Quarterly Journal of the Royal Meteorological Society*, *140*(680), 766–782. https://doi.org/10.1002/qj.2200

Li, L., Zhang, R., & Wen, M. (2017). Genesis of southwest vortices and its relation to Tibetan Plateau vortices. *Quarterly Journal of the Royal Meteorological Society*, *143*(707), 2556–2566. https://doi.org/10.1002/qj.3106

Li, P., Guo, Z., Furtado, K., Chen, H., Li, J., Milton, S., et al. (2019). Prediction of heavy precipitation in the eastern China flooding events of 2016: Added value of convection-permitting simulations. *Quarterly Journal of the Royal Meteorological Society*, *145*(724), 3300–3319. https://doi.org/10.1002/qj.3621

Li, Y., Liu, X., & Chen, B. (2006). Cloud type climatology over the Tibetan Plateau: A comparison of ISCCP and MODIS/TERRA measurements with surface observations. *Geophysical Research Letters*, *33*, L17716. https://doi.org/10.1029/2006GL026890

Liu, L., Zheng, J., Ruan, Z., Cui, Z., Hu, Z., Wu, S., et al. (2015). Comprehensive radar observations of clouds and precipitation over the Tibetan Plateau and preliminary analysis of cloud properties. *Journal of Meteorological Research*, *29*(4), 546–561. https://doi.org/10.1007/s13351-015-4208-6

Liu, Y., Hoskins, B., & Blackburn, M. (2007). Impact of Tibetan orography and heating on the summer flow over Asia. *Journal of the Meteorological Society of Japan*, *85B*, 1–19. https://doi.org/10.2151/jmsj.85B.1

Luo, Y., & Chen, Y. (2015). Investigation of the predictability and physical mechanisms of an extreme-rainfall-producing mesoscale convective system along the Meiyu front in East China: An ensemble approach. *Journal of Geophysical Research: Atmospheres*, *120*, 10,593–10,618. https://doi.org/10.1002/2015JD023584

Luo, Y., Gong, Y., & Zhang, D. (2014). Initiation and organizational modes of an extreme-rain-producing mesoscale convective system along a Mei-Yu front in East China. *Monthly Weather Review*, *142*(1), 203–221. https://doi.org/10.1175/MWR-D-13-00111.1

Luo, Y., Zhang, R., Qian, W., Luo, Z., & Hu, X. (2011). Intercomparison of deep convection over the Tibetan Plateau-Asian monsoon region and subtropical North America in boreal summer using CloudSat/CALIPSO data. *Journal of Climate*, *24*(8), 2164–2177. https://doi.org/10.1175/2010JCLI4032.1

McMurdie, L. A., Rowe, A. K., Houze, R. A., Brodzik, S. R., Zagrodnik, J. P., & Schuldt, T. M. (2018). Terrain-enhanced precipitation processes above the melting layer: Results from OLYMPEX. *Journal of Geophysical Research: Atmospheres*, *123*, 12,194–12,209. https://doi.org/10.1029/2018JD029161

Menzel, P., & Strabala, K. (1997). Cloud top properties and cloud phase algorithm theoretical basis document, University of Wisconsin-Madison.

Molinari, J., & Dudek, M. (1992). Parameterization of convective precipitation in mesoscale numerical models: A critical review. *Monthly Weather Review*, *120*(2), 326–344. https://doi.org/10.1175/1520-0493(1992)120%3C0326:POCPIM%3E2.0.CO;2

Powell, S. W., Houze, R. A., Kumar, A., & McFarlane, S. A. (2012). Comparison of simulated and observed continental tropical anvil clouds and their radiative heating profiles. *Journal of the Atmospheric Sciences*, *69*(9), 2662–2681. https://doi.org/10.1175/JAS-D-11-0251.1

Rasmussen, K. L., & Houze, R. A. (2012). A flash-flooding storm at the steep edge of high terrain disaster in the Himalayas. *Bulletin of the American Meteorological Society*, *93*(11), 1713–1724. https://doi.org/10.1175/BAMS-D-11-00236.1

Sampe, T., & Xie, S. P. (2010). Large-scale dynamics of the Meiyu-Baiu rainband: Environmental forcing by the westerly jet. *Journal of Climate*, *23*(1), 113–134. https://doi.org/10.1175/2009JCLI3128.1

Sun, Y., Dong, X., Cui, W., Zhou, Z., Fu, Z., Zhou, L., et al. (2020). Vertical structures of typical Meiyu precipitation events retrieved from GPM-DPR. *Journal of Geophysical Research: Atmospheres*, *125*, e2019JD031466. https://doi.org/10.1029/2019JD031466

Tao, S., & Ding, Y. (1981). Observational evidence of the influence of the Qinghai-Xizang (Tibet) plateau on the occurrence of heavy rain and severe convective storms on China. *Bulletin of the American Meteorological Society*, *62*(1), 23–30. https://doi.org/10.1175/1520-0477(1981)062%3C0023:OEOTIO%3E2.0.CO;2

Wang, M., Wang, J., Duan, A., Yang, J., & Liu, Y. (2019). Quasi-biweekly impact of the atmospheric heat source over the Tibetan Plateau on summer rainfall in Eastern China. *Climate Dynamics*, *53*(7-8), 4489–4504. https://doi.org/10.1007/s00382-019-04798-x

Wu, G., Liu, Y., He, B., Bao, Q., Duan, A., & Jin, F. (2012). Thermal controls on the Asian summer monsoon. *Scientific Reports*, *2*(1), 404. https://doi.org/10.1038/srep00404

Xu, X., Lu, C., Shi, X., & Gao, S. (2008). World water tower: An atmospheric perspective. *Geophysical Research Letters*, *35*, L20815. https://doi.org/10.1029/2008GL035867

Yan, Y., Liu, Y., & Lu, J. (2016). Cloud vertical structure, precipitation, and cloud radiative effects over Tibetan Plateau and its neighboring regions. *Journal of Geophysical Research: Atmospheres*, *121*, 5864–5877. https://doi.org/10.1002/2015JD024591

Yan, Y., Wang, X., & Liu, Y. (2018). Cloud vertical structures associated with precipitation magnitudes over the Tibetan Plateau and its neighboring regions. *Atmospheric and Oceanic Science Letters*, *11*(1), 44–53. https://doi.org/10.1080/16742834.2018.1395680

Yang, X., Fei, J., Huang, X., Cheng, X., Carvalho, L., & He, H. (2015). Characteristics of mesoscale convective systems over China and its vicinity using geostationary satellite FY2. *Journal of Climate*, *28*(12), 4890–4907. https://doi.org/10.1175/JCLI-D-14-00491.1

Yasunari, T., & Miwa, T. (2006). Convective cloud systems over the Tibetan Plateau and their impact on meso-scale disturbances in the Meiyu/Baiu frontal zone—A case study in 1998. *Journal of the Meteorological Society of Japan*, *84*(4), 783–803. https://doi.org/10.2151/jmsj.84.783

Yu, R., Zhou, T., Xiong, A., Zhu, Y., & Li, J. (2007). Diurnal variations of summer precipitation over contiguous China. *Geophysical Research Letters*, *34*, L01704. https://doi.org/10.1029/2006GL028129

Yuter, S. E., & Houze, R. A. (1995a). Three-dimensional kinematic and microphysical evolution of Florida cumulonimbus. Part II: Frequency distributions of vertical velocity, reflectivity, and differential reflectivity. *Monthly Weather Review*, *123*(7), 1941–1963. https://doi.org/10.1175/1520-0493(1995)123%3C1941:TDKAME%3E2.0.CO;2

Yuter, S. E., & Houze, R. A. (1995b). Three-dimensional kinematic and microphysical evolution of Florida cumulonimbus. Part III: Vertical mass transport, maw divergence, and synthesis. *Monthly Weather Review*, *123*(7), 1964–1983. https://doi.org/10.1175/1520-0493(1995)123%3C1964:TDKAME%3E2.0.CO;2

Zagrodnik, J. P., McMurdie, L. A., & Houze, R. A. (2018). Stratiform precipitation processes in cyclones passing over a coastal mountain range. *Journal of the Atmospheric Sciences*, *75*(3), 983–1004. https://doi.org/10.1175/JAS-D-17-0168.1

Zagrodnik, J. P., McMurdie, L. A., Houze, R. A., & Tanelli, S. (2019). Vertical structure and microphysical characteristics of frontal systems passing over a three-dimensional coastal mountain range. *Journal of the Atmospheric Sciences*, *76*(6), 1521–1546. https://doi.org/10.1175/JAS-D-18-0279.1

Zhang, A., & Fu, Y. (2018). Life cycle effects on the vertical structure of precipitation in East China measured by Himawari-8 and GPM DPR. *Monthly Weather Review*, *146*(7), 2183–2199. https://doi.org/10.1175/MWR-D-18-0085.1

Zhang, A., Fu, Y., Chen, Y., Liu, G., & Zhang, X. (2018). Impact of the surface wind flow on precipitation characteristics over the southern Himalayas: GPM observations. *Atmospheric Research*, *202*, 10–22. https://doi.org/10.1016/j.atmosres.2017.11.001

Zhang, D., Hsie, E. Y., & Moncrieff, M. W. (1988). A comparison of explicit and implicit predictions of convective and stratiform precipitating weather systems with a meso-beta-scale numerical model. *Quarterly Journal of the Royal Meteorological Society*, *114*, 31–60.

Zhang, D., Kain, J. S., Fritsch, J. M., & Gao, K. (1994). Comments on "parameterization of convective precipitation in mesoscale numerical models: A critical review". *Monthly Weather Review*, *122*(9), 2222–2231. https://doi.org/10.1175/1520-0493(1994)122%3C2222:COOCPI%3E2.0.CO;2

Zhao, Y., Xu, X., Liu, L., Zhang, R., Xu, H., Wang, Y., & Li, J. (2019). Effects of convection over the Tibetan Plateau on rainstorms downstream of the Yangtze River Basin. *Atmospheric Research*, *219*, 24–35. https://doi.org/10.1016/j.atmosres.2018.12.019

Zhou, C., Wang, K., & Qi, D. (2018). Attribution of the July 2016 extreme precipitation event over China's Wuhan. *Bulletin of the American Meteorological Society*, *99*(1), S107–S112. https://doi.org/10.1175/BAMS-D-17-0090.1

Zhou, T., Yu, R., Zhang, J., Drange, H., Cassou, C., Deser, C., et al. (2009). Why the western Pacific subtropical high has extended westward since the late 1970s. *Journal of Climate*, *22*(8), 2199–2215. https://doi.org/10.1175/2008JCLI2527.1